



Title	Oxygen and Al-Mg isotopic constraints on cooling rate and age of partial melting of an Allende Type B CAI, Golfball
Author(s)	Kawasaki, Noriyuki; Itoh, Shoichi; Sakamoto, Naoya; Simon, Steven B.; Yamamoto, Daiki; Yurimoto, Hisayoshi
Citation	Meteoritics & Planetary Science, 56(6), 1224-1239 https://doi.org/10.1111/maps.13701
Issue Date	2021-07
Doc URL	http://hdl.handle.net/2115/86240
Rights	This is the peer reviewed version of the following article: Meteoritics & planetary science, vol.56 no.6 pp.1224-1239, which has been published in final form at https://doi.org/10.1111/maps.13701 . This article may be used for non-commercial purposes in accordance with Wiley Terms and Conditions for Use of Self-Archived Versions.
Type	article (author version)
File Information	Meteorit. Planet. Sci. 56-6_1224-1239.pdf



[Instructions for use](#)

1 **Oxygen and Al–Mg isotopic constraints on cooling rate and age of partial melting**
2 **of an Allende Type B CAI, Golfball**

3
4 Noriyuki Kawasaki ^{a,*}, Shoichi Itoh ^b, Naoya Sakamoto ^c, Steven B. Simon ^d,
5 Daiki Yamamoto ^e and Hisayoshi Yurimoto ^{a,c}

6
7 *^aDepartment of Natural History Sciences, Hokkaido University, Sapporo 060-0810,*
8 *Japan*

9 *^bDepartment of Earth and Planetary Sciences, Kyoto University, Kyoto 606-8502,*
10 *Japan*

11 *^cIsotope Imaging Laboratory, Creative Research Institution, Hokkaido University,*
12 *Sapporo 001-0021, Japan*

13 *^dInstitute of Meteoritics, University of New Mexico, Albuquerque, New Mexico 87131,*
14 *USA*

15 *^eInstitute of Space and Astronautical Science, Japan Aerospace Exploration Agency,*
16 *Sagamihara 252-5210, Japan.*

17
18 *Corresponding author. Email: kawasaki@ep.sci.hokudai.ac.jp

19
20 **Keywords:** Ca-Al-rich inclusions; partial melting; oxygen isotopes; Al–Mg systematics

21

ABSTRACT

22

23 Coarse-grained, igneous Ca-Al-rich inclusions (CAIs) in CV chondrites formed through
24 multiple melting events. We conducted *in situ* O-isotope analysis and Al–Mg systematics
25 by secondary ion mass spectrometry of relict and overgrown minerals from a partial
26 melting event in an Allende Type B CAI, Golfball. Golfball has a Type B CAI bulk
27 composition and a unique structure: a fassaite-rich mantle enclosing a melilite-rich core.
28 Many of the blocky melilite crystals in the core have irregularly-shaped, Al-rich (Åk_{5–15})
29 cores enclosed in strongly zoned (Åk_{30–70}) overgrowths. Since the Al-rich melilite grains
30 could not have formed from a melt of Golfball, they are interpreted as relict grains that
31 survived later melting events. The O-isotopic compositions of the blocky melilite crystals
32 plot along the carbonaceous chondrite anhydrous mineral line, ranging between $\Delta^{17}\text{O} \sim$
33 -14% and -5% . The Al-rich relict melilite grains and their overgrowths exhibit the same
34 O-isotopic compositions, while the O-isotopic compositions are varied spatially among
35 melilites. We found that the O-isotopic compositions steeply change across several
36 melilite crystals within few tens of micrometers, indicating the O-isotopic compositions
37 of the melt could not have been homogenized during the partial melting in that scale.
38 According to the timescale of O self-diffusivity in the melt, the cooling rate of the partial
39 melting event is calculated to be $> 6 \times 10^4$ K/h. Al–Mg isotope data for core minerals plot
40 on a straight line on an Al–Mg evolution diagram. A mineral isochron for Golfball gives
41 initial $^{26}\text{Al}/^{27}\text{Al}$ of $(4.42 \pm 0.20) \times 10^{-5}$ and initial $\delta^{26}\text{Mg}^*$ of $-0.035 \pm 0.050\%$. The
42 chemical and O-isotopic compositions of melilite and those initial values imply that its
43 precursor consisted of fluffy Type A and/or fine-grained CAIs. The partial melting event
44 for Golfball may have occurred in very short order after the precursor formation.

45

1. INTRODUCTION

46

47 Ca-Al-rich inclusions (CAIs) in chondrites are the oldest objects formed in the
48 Solar System (Connelly et al., 2012). Coarse-grained, compact Type A, Type B, and Type
49 C CAIs in CV chondrites experienced melting and solidification and are thus igneous in
50 origin (e.g., MacPherson and Grossman, 1981; Wark and Lovering, 1982; Wark, 1987;
51 Simon et al., 1999). They exhibit unequilibrated O-isotopic compositions distributed
52 along the carbonaceous chondrite anhydrous mineral (CCAM) line, a nearly slope-1 line
53 on an O three-isotope diagram (Clayton et al., 1977; Clayton, 1993). Coarse-grained,
54 igneous CAIs have been suggested to have experienced multiple melting events, based
55 on their petrography and chemical and O-isotopic distributions (MacPherson and Davis,
56 1993; Yurimoto et al., 1998; Beckett et al., 2000; Ito et al., 2004; Simon et al., 2005;
57 Yoshitake et al., 2005; Aléon et al., 2007; Krot et al., 2008a; Wakaki et al., 2013; Aléon,
58 2016; Kawasaki et al., 2015, 2018).

59 Most CAIs contained ^{26}Al , a short-lived radionuclide with a half-life of 0.705
60 Myr (Norris et al., 1983), at the time of their formation (e.g., Lee et al., 1976; MacPherson
61 et al., 1995). The Al–Mg systematics of individual CAIs in CV chondrites revealed that
62 coarse-grained, igneous CAIs and condensate CAIs, such as fluffy Type A (FTAs) and
63 fine-grained CAIs (FGIs), exhibit similar variations in initial $^{26}\text{Al}/^{27}\text{Al}$ values, $(^{26}\text{Al}/^{27}\text{Al})_0$
64 (e.g., MacPherson et al., 2010, 2012, 2017; Kita et al., 2012; Kawasaki et al., 2019, 2020);
65 the processes of condensation and melting for CAI formation occurred
66 contemporaneously during the first ~ 0.4 Myr of the Solar System formation (Kawasaki
67 et al., 2020). Formation events of Type C CAIs may be related to chondrule formation,
68 and their inferred low $(^{26}\text{Al}/^{27}\text{Al})_0$ imply their last melting events occurred $> \sim 2$ Myr after
69 formation of most CAIs (e.g., Krot et al., 2005, 2007; Kawasaki et al., 2015). However,

70 it is still debatable whether variations in $(^{26}\text{Al}/^{27}\text{Al})_0$ among CAIs correspond to a
71 formation age spread or heterogeneous distributions of ^{26}Al in the forming region (e.g.,
72 Wasserburg et al., 1977; Krot et al., 2008b; Jacobsen et al., 2008; Larsen et al., 2011,
73 2020; Makide et al., 2011; Holst et al., 2013; Kööp et al., 2016; Park et al., 2017;
74 Kawasaki et al., 2019, 2020).

75 The Al–Mg systematics recorded by multiple partial melting events of individual
76 igneous CAIs would constrain age differences between the melting and precursor
77 formation events, regardless of the possibility of heterogeneous distributions of ^{26}Al .
78 Internal, partial resetting of Al–Mg system of CAIs by partial melting has been suggested
79 by several studies (Podosek et al., 1991; Hsu et al., 2000; MacPherson et al., 2012, 2018;
80 Kawasaki et al., 2015). Ito et al. (2006) and Kawasaki et al. (2015) investigated the
81 Al–Mg systematics of relict minerals and minerals that crystallized as a result of partial
82 melting events, determined based on their petrography and O-isotope disequilibrium. The
83 Al–Mg data for the relict melilite and later-crystallized melilite in an Allende compact
84 Type A CAI 7R-19-1 do not show a resolvable age difference between them (Ito et al.,
85 2006), although the analytical error of ~ 0.4 Myr is comparable to the inferred formation
86 period of CV CAIs (Kawasaki et al., 2020). On the other hand, internal resetting of the
87 Al–Mg system is demonstrated for an Allende Type C CAI, EK1-04-2, in which relict
88 spinel grains and later-crystallized minerals from a partial melting event have a relative
89 age difference of at least ~ 1.6 Myr (Kawasaki et al., 2015).

90 In this study, we determined the Al–Mg systematics of relict minerals and later-
91 crystallized minerals from a partial melting event in an Allende Type B CAI, Golfball
92 (Simon et al., 2005) by secondary ion mass spectrometry (SIMS). This CAI has a Type B
93 CAI bulk composition (Simon and Grossman, 2004) and a unique structure of a thin

94 melilite mantle at the outermost edge, and a thicker fassaite-rich mantle enclosing a
95 melilite-rich core (Fig. 1). It shows a clear signature of partial melting; Al-rich relict
96 melilite grains (\AA k_{5-15}) surrounded by strongly zoned
97 overgrowths (\AA k_{30-70}) are present in the core. In addition, we conducted *in situ* O-isotope
98 analyses of the relict and overgrown melilites by SIMS. Based on disequilibrium
99 distributions of O-isotopic compositions in melilite crystals, we constrain a cooling rate
100 of the partial melting event. Preliminary results of O and Al–Mg isotope analyses of
101 minerals in Golfball were reported by Itoh et al. (2009).

102

103

2. EXPERIMENTAL TECHNIQUES

104 2.1 Sample preparation and elemental analysis

105 The polished thin section of the Allende Type B CAI Golfball, section GBL2
106 (Simon et al., 2005), was coated with a carbon thin film (~20 nm) for backscattered
107 electron (BSE) imaging, elemental analysis using an energy dispersive X-ray
108 spectrometer (EDS), crystal orientation mapping using an electron backscatter diffraction
109 (EBSD) system and O-isotope spot analysis by SIMS, and it was coated with a gold thin
110 film (~70 nm) for O-isotope imaging and Al–Mg isotope analysis by SIMS.

111 BSE images were obtained using a field emission type scanning electron
112 microscope (FE-SEM; JEOL JSM-7000F) at Hokkaido University. Quantitative X-ray
113 elemental mapping was conducted using an EDS (Oxford X-Max 150) installed on the
114 FE-SEM. A 15 keV electron beam probe with currents of 10 nA was employed. The
115 \AA k_{5-15} contents of O-isotope spot analysis locations in melilite were extracted from
116 the quantitative \AA k_{5-15} content map. Statistical error of the \AA k_{5-15} contents of
117 melilite extracted from an area of 2–3 μm , which corresponds to probe sizes of the SIMS

118 analysis, was less than 2 mol% (2σ). Grain boundaries of melilite crystals were
119 determined using an EBSD system (Oxford Aztec HKL) on the FE-SEM. A 20 keV
120 electron beam probe with currents of 4 nA was employed.

121 **2.2 Oxygen isotope spot analysis**

122 O-isotopic compositions for the minerals in Golfball were measured using a
123 SIMS instrument (Cameca ims-1280HR) of Hokkaido University, following the
124 analytical procedures reported in Kawasaki et al. (2018). A $^{133}\text{Cs}^+$ primary beam (20 keV,
125 ~ 30 pA) with a diameter of 2–3 μm was used. Negative secondary ions ($^{16}\text{O}^-$, $^{17}\text{O}^-$, and
126 $^{18}\text{O}^-$) were measured simultaneously in the multicollection mode. $^{16}\text{O}^-$, $^{17}\text{O}^-$, and $^{18}\text{O}^-$
127 were measured using a multicollector Faraday cup (10^{11} Ω , designed for L1), an axial
128 electron multiplier, and a multicollector electron multiplier (designed for H2),
129 respectively. A normal-incidence electron flood gun was used for electrostatic charge
130 compensation of the analyzing areas during the measurements. The mass resolution of
131 $M/\Delta M$ for $^{17}\text{O}^-$ was set at ~ 6000 to ensure that the contribution of $^{16}\text{OH}^-$ to $^{17}\text{O}^-$ is
132 negligible, while that for $^{16}\text{O}^-$ and $^{18}\text{O}^-$ was ~ 2000 . The secondary ion intensity of $^{16}\text{O}^-$
133 was $\sim 2 \times 10^7$ cps. Each measurement was conducted with 30 cycles of counting the
134 secondary ions for 4 s. Obtained count rates were corrected for FC background, EM
135 deadtime, and relative yield of each detector. Synthetic gehlenite ($\delta^{18}\text{O} = 7.4\text{‰}$) and
136 Russian spinel ($\delta^{18}\text{O} = 8.5\text{‰}$) (Yurimoto et al., 1994) were used as standards to correct
137 instrumental mass fractionation for the CAI melilite and spinel, respectively. Analytical
138 errors include an internal error of individual analysis and an uncertainty of the
139 instrumental mass fractionation (assigned as 2SE of repetitive analyses of the standards).
140 Typical errors for $\delta^{17}\text{O}$, $\delta^{18}\text{O}$, and $\Delta^{17}\text{O}$ were 2.2‰, 1.0‰, and 2.3‰ (2σ), respectively.

141 **2.3 Oxygen isotope imaging**

142 Quantitative O-isotope imaging was conducted using an isotope microscope
143 system (Cameca ims-1270e7 with SCAPS) of Hokkaido University (Yurimoto et al.,
144 2003), following the analytical and data reduction procedures reported in Park et al.
145 (2012) and Matsuda et al. (2019). A $^{133}\text{Cs}^+$ primary beam (15 keV, ~ 2 nA) was uniformly
146 irradiated onto the sample surface as an oval shape with a traverse diameter of ~ 70 μm .
147 A normal-incidence electron flood gun was used for the electrostatic charge compensation
148 of the analyzing area. The contrast aperture of 150 μm was used. The energy slit and exit
149 slit widths were set to 50 μm and 750 μm , respectively. After the pre-sputtering, secondary
150 ion images were acquired using the following sequences and acquisition times in the order
151 of $^{27}\text{Al}^{16}\text{O}^-$ for 50 s, $^{16}\text{O}^-$ for 5 s, $^{18}\text{O}^-$ for 200 s, $^{16}\text{O}^-$ for 5 s, $^{18}\text{O}^-$ for 200 s, $^{16}\text{O}^-$ for 5 s,
152 $^{18}\text{O}^-$ for 200 s, and $^{16}\text{O}^-$ for 5 s. The calculated $^{18}\text{O}^-/^{16}\text{O}^-$ secondary ion ratio image was
153 converted to the SMOW scale by normalization using the data of O-isotope spot analysis
154 (#612–615, #617 and #618).

155 **2.4 Al–Mg isotope analysis in multicollection mode**

156 Mg-isotopic compositions and $^{27}\text{Al}/^{24}\text{Mg}$ ratios of the minerals in Golfball were
157 measured using the SIMS instrument (Cameca ims-1280HR) of Hokkaido University,
158 following the analytical procedures reported in Kawasaki et al. (2019, 2020). An $^{16}\text{O}^-$
159 primary beam accelerated to 23 keV was employed in the experiment. We used both the
160 peak-jumping mode and the multicollection mode, depending on the secondary ion
161 intensities of Mg-isotopes from the minerals. For Mg-rich melilite ($^{27}\text{Al}/^{24}\text{Mg} < 7$) and
162 spinel, the Mg-isotopes ($^{24}\text{Mg}^+$, $^{25}\text{Mg}^+$, and $^{26}\text{Mg}^+$) and $^{27}\text{Al}^+$ were measured
163 simultaneously in the multicollection mode with four Faraday cups: $^{24}\text{Mg}^+$ for L2* (10^{11}
164 Ω), $^{25}\text{Mg}^+$ for L1 (10^{11} Ω), $^{26}\text{Mg}^+$ for H1 (10^{11} Ω), and $^{27}\text{Al}^+$ for H2* (10^{10} Ω). The primary
165 beam was set to 25–28 nA with an almost circular shape of ~ 19 μm for the Mg-rich

166 melilite measurements and ~ 6 nA with an elliptical shape of $7 \times 11 \mu\text{m}$ for the spinel
167 measurements. The mass resolution of $M/\Delta M$ was set at ~ 2000 . The contributions of ion
168 interferences (e.g., $^{48}\text{Ca}^{2+}$, $^{24}\text{MgH}^+$, $^{25}\text{MgH}^+$, and $^{52}\text{Cr}^{2+}$) were negligible under these
169 conditions. The secondary ion intensities of $^{24}\text{Mg}^+$ were $1.1\text{--}1.3 \times 10^8$ and $\sim 2.4 \times 10^8$ cps
170 for Mg-rich melilite and spinel, respectively. Each measurement was conducted with 20
171 cycles of counting the secondary ions for 10 s. Obtained count rates were corrected for
172 FC background and relative yield of each detector. The relative sensitivity factors for Al
173 and Mg were determined through measurements of synthetic melilite glasses and Russian
174 spinel for melilite and spinel, respectively. The mass-dependent fractionations of Mg-
175 isotopes for the minerals in Golfball are reported as $\delta^{25}\text{Mg}_{\text{DSM3}}$ values (permil deviation
176 from Mg reference material DSM-3; Galy et al., 2003). The $\delta^{25}\text{Mg}_{\text{DSM3}}$ for the synthetic
177 melilite glasses is $-1.76 \pm 0.13\text{‰}$ measured with multi-collector inductively coupled
178 plasma-mass spectrometry (MC-ICP-MS), and they are used for the corrections of
179 melilite in Golfball. The $\delta^{25}\text{Mg}_{\text{DSM3}}$ value for Russian spinel was assumed to be zero for
180 the correction of spinel in Golfball.

181 The excess of radiogenic ^{26}Mg , $\delta^{26}\text{Mg}^*$, was calculated via an exponential
182 fractionation law with coefficient $\alpha_{\text{natural}} = 0.5128$ because natural fractionation for Mg-
183 isotopes is considered to be controlled by evaporation processes (Davis et al., 2015).
184 However, the natural mass fractionation deviates from the instrumental mass fractionation
185 of SIMS, and the instrumental mass fractionation also differs among target minerals and
186 among analytical sessions under the measurement conditions (Itoh et al., 2008; Kawasaki
187 et al., 2017, 2018, 2019, 2020). We determined instrumental mass fractionation, α_{SIMS} ,
188 through measurements of terrestrial standards to calculate the excess radiogenic ^{26}Mg in
189 each analytical session. The α_{SIMS} values for Mg-rich melilite and spinel were determined

190 via linear regressions of the $\Phi^{25}\text{Mg}$ and $\Phi^{26}\text{Mg}$ values of Takashima augite and each of
 191 the standard, the synthetic melilite glasses and Russian spinel, respectively, where
 192 $\Phi^{25,26}\text{Mg} = 1000 \times \ln [({}^{25,26}\text{Mg}/{}^{24}\text{Mg})_{\text{sample}}/({}^{25,26}\text{Mg}/{}^{24}\text{Mg})_{\text{ref.}}]$. The terrestrial reference
 193 ratios of $({}^{25}\text{Mg}/{}^{24}\text{Mg})_{\text{ref.}} = 0.12663$ and $({}^{26}\text{Mg}/{}^{24}\text{Mg})_{\text{ref.}} = 0.13932$ (Catanzaro et al., 1966)
 194 were used for $\delta^{26}\text{Mg}^*$ calculations, although the final corrected $\delta^{26}\text{Mg}^*$ values are
 195 independent of the reference ratios used. In this study, the α_{SIMS} for Mg-rich melilite were
 196 found to be 0.498 ± 0.002 (2σ), 0.498 ± 0.003 and 0.501 ± 0.002 for different three
 197 sessions and the α_{SIMS} for spinel were 0.513 ± 0.002 and 0.516 ± 0.003 for different two
 198 sessions. From the results of the linear regressions, an instrumental offset for the $\delta^{26}\text{Mg}^*$
 199 values, β , which ranged from -0.50 to -0.54 with errors of 0.01 – 0.02 depending on
 200 minerals and analytical sessions, was identified. The fractionation-corrected $\delta^{26}\text{Mg}^*$
 201 values for CAI minerals were determined by the following equation

$$\begin{aligned} \delta^{26}\text{Mg}^* = & \delta^{26}\text{Mg}_{\text{sample}} - \left[\left(1 + \frac{\delta^{25}\text{Mg}_{\text{sample}}}{1000} \right)^{\frac{1}{\alpha_{\text{natural}}}} - 1 \right] \times 1000 \\ & - \beta + \left[\left(1 + \frac{\delta^{25}\text{Mg}_{\text{std}}}{1000} \right)^{\frac{1}{\alpha_{\text{natural}}}} - 1 \right] \times 1000 \\ & - \left[\left(1 + \frac{\delta^{25}\text{Mg}_{\text{std}}}{1000} \right)^{\frac{1}{\alpha_{\text{SIMS}}}} - 1 \right] \times 1000, \end{aligned}$$

202 where $\delta^{25,26}\text{Mg}_{\text{sample}} = [({}^{25,26}\text{Mg}/{}^{24}\text{Mg})_{\text{sample}}/({}^{25,26}\text{Mg}/{}^{24}\text{Mg})_{\text{ref.}} - 1] \times 1000$, $\delta^{25}\text{Mg}_{\text{std}} =$
 203 $[({}^{25}\text{Mg}/{}^{24}\text{Mg})_{\text{std}}/({}^{25}\text{Mg}/{}^{24}\text{Mg})_{\text{ref.}} - 1] \times 1000$. More details and the error estimation
 204 procedure are described elsewhere (Kawasaki et al., 2017). The analytical errors (2σ) for
 205 $\delta^{26}\text{Mg}^*$ were $\sim 0.13\text{‰}$ for Mg-rich melilite and $\sim 0.07\text{‰}$ for spinel.

206 2.5 Al–Mg isotope analysis in peak-jumping mode

207 For Mg-poor melilite ($^{27}\text{Al}/^{24}\text{Mg} > 16$), Mg-isotopes ($^{24}\text{Mg}^+$, $^{25}\text{Mg}^+$, and $^{26}\text{Mg}^+$)
208 were measured using an axial electron multiplier, while $^{27}\text{Al}^+$ was measured using a
209 multicollector Faraday cup ($10^{11} \Omega$, designed for H2*) simultaneously with $^{25}\text{Mg}^+$, in
210 peak-jumping mode. An $^{16}\text{O}^-$ primary beam accelerated to 23 keV was employed in the
211 experiment. The primary beam current was set to ~ 140 pA with an elliptical shape of $3 \times$
212 $5 \mu\text{m}$. The mass resolution of $M/\Delta M$ was set at ~ 4000 , which is sufficient to resolve ion
213 interferences (e.g., $^{48}\text{Ca}^{2+}$, $^{24}\text{MgH}^+$, $^{25}\text{MgH}^+$, and $^{52}\text{Cr}^{2+}$). The secondary ion intensities of
214 $^{24}\text{Mg}^+$ were $0.1\text{--}1.5 \times 10^5$ cps. Each measurement was conducted for 100 cycles with a
215 counting sequence with $^{24}\text{Mg}^+$ for 2 s, $^{25}\text{Mg}^+$ for 2 s, $^{25}\text{Mg}^+$ and $^{27}\text{Al}^+$ for 4 s, and $^{26}\text{Mg}^+$
216 for 6 s. The obtained count rates were corrected for the FC background and EM deadtime.
217 The instrumental mass fractionation and relative sensitivity factor for Al and Mg were
218 determined through measurements of synthetic melilite glasses. The calculation methods
219 of $\delta^{26}\text{Mg}^*$ and $\delta^{25}\text{Mg}_{\text{DSM3}}$ are essentially identical to those described in Section 2.4
220 although α_{SIMS} and β were not determined in the peak-jumping mode because the
221 instrumental mass fractionation and natural mass fractionation were indistinguishable
222 from each other under the measurement conditions here. The analytical errors for $\delta^{26}\text{Mg}^*$
223 were assigned as internal errors (2SE) and were 1.1–1.7%.

224

225

3. RESULTS

3.1 Mineralogy and petrology

227

228

229

230

Fig. 1 shows BSE and elemental maps of Golfball, section GBL2, which has a rounded shape with a diameter of ~ 7 mm. Detailed petrography and mineral chemistry of Golfball are presented in Simon et al. (2005). The bulk chemical composition of Golfball was determined by a modal recombination technique by Simon and Grossman (2004),

231 showing a Type B CAI bulk composition. Golfball has a core-mantle structure of a
232 melilite-rich core enclosed by a fassaite-rich mantle and a relatively thin outermost
233 melilite mantle, which has not been observed in other Type B CAIs. Some melilite laths
234 appear to have nucleated on the edge of the CAI and then grew inward (Simon et al.,
235 2005).

236 The melilite-rich core is mainly composed of blocky melilite crystals with sizes
237 typically 20–50 μm across (Fig. 2), plus several lathlike melilite crystals protruding from
238 the core into the mantle (Fig. 3a). The blocky melilite crystals enclose many small spinel
239 crystals and are separated by pockets of fassaite, spinel, and rare anorthite. Fassaite
240 crystals with sizes of ~ 1 mm across (Fig. 1d) poikilitically enclose the blocky melilite and
241 spinel crystals (Fig. 2a). The blocky melilite crystals are very strongly concentrically
242 zoned; they exhibit typically normal zoning from $\sim \text{Åk}_{30}$ to $\sim \text{Åk}_{70}$, but some have Mg-rich
243 cores (up to $\sim \text{Åk}_{60}$) to form oscillatory zoning (Fig. 2). They also often contain irregularly
244 shaped Al-rich cores, typically $\sim \text{Åk}_{5-15}$, enclosed in strongly zoned overgrowths
245 (typically $\sim \text{Åk}_{30-70}$) (Figs. 2 and 4; Figs. 4 and 5 of Simon et al. 2005). The thin
246 transitional zones observed between the Al-rich grains and the overgrowths were reported
247 to be ~ 5 μm wide inferred from the electron microprobe traverse (Fig. 5 of Simon et al.
248 2005), but new data for many Al-rich grains, after the careful examination of X-ray
249 mapping in this study, indicate that the width of transitional zones is ~ 1 μm (e.g., Fig. 4d),
250 which is slightly larger than the spatial resolution of 0.6 μm estimated for the EDS line
251 profile from a boundary between spinel and melilite defined by the width between the
252 16% and 84% level. The wider transitional zones of the previous study may be due to
253 fluorescence effects of X-ray generation by slanting grain boundaries.

254 The fassaite-rich mantle is ~ 1 mm thick and mainly composed of fassaite and

255 spinel. The subhedral to nearly euhedral, mantle fassaite crystals poikilitically enclose
256 abundant spinel crystals. Primary, anhedral anorthite crystals occur typically adjacent to
257 the fassaite crystals. At the outer edge of the inclusion, radially oriented melilite laths
258 occur (Figs. 1 and 3b; Fig. 1d of Simon et al. 2005). The lath melilite crystals in the rim
259 are $\sim 500 \mu\text{m}$ long and show inward growth zoning from $\sim \text{Åk}_{30}$ to $\sim \text{Åk}_{70}$, and then back
260 to $\sim \text{Åk}_{50}$, probably due to the onset of cocrystallization with fassaite (MacPherson et al.,
261 1984).

262 **3.2 O-isotopic compositions**

263 The measured O-isotopic compositions of minerals in Golfball and locations of
264 SIMS measurements are summarized in Supplementary materials. Fig. 5 shows the O-
265 isotopic compositions plotted on the O three-isotope diagram. The O-isotopic
266 compositions of minerals are distributed along the CCAM line within error. Compositions
267 range between $\Delta^{17}\text{O} \sim -23\text{‰}$ and -5‰ , which shows O-isotope disequilibrium in the
268 CAI.

269 The spinel in the core exhibits homogeneously ^{16}O -rich compositions ($\Delta^{17}\text{O} =$
270 $-24.0 \pm 1.9\text{‰}$, 2SD), despite their different petrographic settings (Table 1). On the other
271 hand, O-isotopic compositions of the blocky melilite crystals in the core exhibit
272 significant variations, ranging from $\Delta^{17}\text{O} \sim -14$ to -5‰ (Fig. 5).

273 The O-isotopic compositions of blocky melilite crystals in various areas are
274 shown in Fig. 6. The O-isotopic compositions are not correlated with åkermanite contents
275 (i.e., crystal growth), but show various distributions in each area. The melilites in the
276 areas 1 to 3 exhibit compact $\Delta^{17}\text{O}$ distributions, but the average $\Delta^{17}\text{O}$ for area 3 ($\Delta^{17}\text{O} =$
277 $-6.4 \pm 2.1\text{‰}$) is slightly ^{16}O -poorer than those for areas 1 ($-9.0 \pm 2.0\text{‰}$) and 2 ($-9.4 \pm$
278 2.0‰). There are no resolvable differences in O-isotopic compositions between the Al-

279 rich cores and the overgrowths in each area. The quantitative $\delta^{18}\text{O}$ image of a blocky
280 melilite crystal containing Al-rich grain (Fig. 4f) clearly shows that O-isotopic
281 composition is homogeneous within the whole crystal, supporting the characteristics
282 shown in Figs. 6a to 6f. In area 4, the O-isotopic compositions of Al-rich grains are also
283 identical to those of the most overgrown grains ($\Delta^{17}\text{O} \sim -8\text{‰}$), while the average $\Delta^{17}\text{O}$ is
284 intermediate among those of the areas 1 to 3. Moreover, some overgrowths are slightly
285 enriched in ^{16}O ($\Delta^{17}\text{O} \sim -10\text{‰}$). The O-isotopic compositions of melilite in area 5 show
286 significant variations, ranging from $\Delta^{17}\text{O} \sim -14$ to -8‰ . Fig. 7 shows the O-isotopic
287 compositions ($\delta^{18}\text{O}$) of melilite grains in area 5. The O-isotopic compositions are not
288 randomly distributed among measurement sites, but instead show long range patterns
289 across numerous grains.

290 **3.3 Al-Mg isotopic compositions**

291 The Mg-isotopic compositions and $^{27}\text{Al}/^{24}\text{Mg}$ ratios measured for minerals in
292 Golfball are summarized in Table 2. Fig. 8 shows the Mg-isotopic compositions and
293 $^{27}\text{Al}/^{24}\text{Mg}$ ratios of minerals in the core of Golfball plotted on the ^{26}Al - ^{26}Mg evolution
294 diagrams. The Al-Mg isotope data perfectly plot on a straight line. If we define an
295 ^{26}Al - ^{26}Mg mineral isochron, the isochron gives initial values of $(^{26}\text{Al}/^{27}\text{Al})_0 = (4.42 \pm$
296 $0.20) \times 10^{-5}$ and initial $\delta^{26}\text{Mg}^*$, $(\delta^{26}\text{Mg}^*)_0 = -0.035 \pm 0.050\text{‰}$.

297 Averages of $\delta^{25}\text{Mg}_{\text{DSM3}}$ values for Al-rich melilite grains, overgrown melilite
298 grains, and spinel are $1.4 \pm 1.5\text{‰}$ (2SD, $n = 12$), $1.8 \pm 0.2\text{‰}$ ($n = 3$) and $1.79 \pm 0.13\text{‰}$ (n
299 $= 6$), respectively. These $\delta^{25}\text{Mg}_{\text{DSM3}}$ values by SIMS are consistent with the bulk Mg-
300 isotopic composition for Golfball, $\delta^{25}\text{Mg}_{\text{DSM3}} = 1.61 \pm 0.06\text{‰}$ (Grossman et al., 2008),
301 measured by MC-ICP-MS.

302

4. DISCUSSION

4.1 Cooling rate of partial melting event inferred from O-isotopic distributions

As discussed in Simon et al. (2005), the Al-rich grains in blocky melilite crystals in Golfball could not have crystallized from a liquid having chemical composition of bulk Golfball or even that of its core (Simon and Grossman, 2004), according to the inferred initial melilite compositions crystallized from a CMAS melt (Beckett et al., 1999). Thus, they are relict grains that survived partial melting events (see also Fig. 11 of Simon et al. 2005). The Al-rich relict grains and the surrounding overgrown melilite grains in areas 1 to 3 have the same O-isotopic composition as each other (Figs. 4f, 6a, 6c and 6e), indicating O-isotopes of the overgrown melilite grains are inherited from those of precursor materials. Moreover, the O-isotopic compositions of melilite exhibit spatial variations as observed in areas 4 and 5 (Figs. 6g, 6i and 7). Because the O-isotopic compositions of melilite crystals are not correlated with their åkermanite contents (i.e., crystal growth) (Fig. 6), the O-isotopic variations cannot be attributed to a temporal change of O-isotopic composition of the melt during cooling after the partial melting events.

Fig. 9 shows O-isotopic compositions along a linear traverse across melilite crystals in area 5 (Fig. 7). The O-isotopic compositions of melilite crystals steadily change within a zone of $\sim 21 \mu\text{m}$ width while the first $40 \mu\text{m}$ and the last $40 \mu\text{m}$ of the traverse exhibit almost flat distributions of O-isotopic compositions, with $\delta^{18}\text{O} \sim -20\text{‰}$ and $\delta^{18}\text{O} \sim -12\text{‰}$, respectively. Because those flat distributions could be inheritance of the isotopic variations of precursor materials having $\delta^{18}\text{O}$ of $\sim -20\text{‰}$ and $\sim -12\text{‰}$, the monotonic change zone could have been formed by O-isotope diffusion in the melt during partial melting. The diffusion distance $((Dt)^{1/2}$, D : diffusion coefficient, t : time) of O-

327 isotope in the melt can be determined to be $\sim 11 \mu\text{m}$, using a diffusion model with the
328 initial condition of two semi-infinite sources (Shewmon, 1963). The heterogeneity of O-
329 isotopic compositions strongly suggests that O-isotope exchange between the melt and
330 surrounding nebular gas, as suggested for many coarse-grained CAIs (e.g., Yurimoto et
331 al., 1998; Kawasaki et al., 2018), did not occur during crystallization of these melilites in
332 Golfball. The lack of the gas-melt O-isotope exchange was also suggested for other CAIs
333 (Aléon, 2016, 2018).

334 To preserve the O-isotope gradient in the melt inherited from precursor materials
335 during the partial melting event, melilite crystallization accompanied by cooling must
336 have been completed prior to homogenization of O-isotopes. A cooling rate after the
337 heating that caused the partial melting event can be estimated from the diffusion distance,
338 applying a non-isothermal diffusion model (Lasaga, 1983) and the inferred maximum
339 temperature, $\sim 1400^\circ\text{C}$, of the early partial melting event (step 1 of Fig. 11 of Simon et al.
340 2005). Using an O self-diffusion coefficient of $1.62 \times 10^{-7} \text{ cm}^2 \text{ sec}^{-1}$ at 1420°C for a CAIB
341 melt (Yamamoto et al., 2019) and an activation energy of 170 kJ/mol for O self-diffusion
342 in dry basaltic liquid (Leshner et al., 1996), a cooling rate for the O self-diffusion distance
343 of $11 \mu\text{m}$ is estimated to be $6 \times 10^4 \text{ K/h}$. The cooling rate could be faster than $6 \times 10^4 \text{ K/h}$
344 if the original O-isotopic variations of precursor materials contribute to the observed O-
345 isotope gradient. Such gradual O-isotopic compositions have been observed in melilite
346 crystals of Type A CAIs (Katayama et al., 2012; Kawasaki et al., 2012; Park et al., 2012).
347 In addition, if the solid-state diffusion of O-isotopes occurred during the later partial
348 melting event and thermal metamorphism on the parent body, the O self-diffusion
349 distance in the melt would be shorter than $11 \mu\text{m}$. If this is the case, then the cooling rate
350 could be faster than $6 \times 10^4 \text{ K/h}$.

351 The estimated cooling rate of $> 6 \times 10^4$ K/h is much faster than those inferred for
352 CAIs, $\sim 0.5\text{--}50$ K/h from experimental studies (MacPherson et al., 1984; Stolper and
353 Paque, 1986) and $< \sim 1$ K/h from a natural CAI (Kawasaki et al., 2018). That is even faster
354 than those for chondrules from experimental studies ($\sim 1\text{--}3000$ K/h: Jones et al., 2018 and
355 references therein) but slower than those inferred from a natural chondrule ($10^5\text{--}10^6$ K/h:
356 Yurimoto and Wasson, 2002). Although Golfball has a Type B CAI bulk composition, its
357 mineral textures are quite unlike other Type B CAIs. Therefore, the cooling rates inferred
358 for other CAIs may not be applied to this early heating event, in which the Golfball
359 precursors were partially melted. A later heating event, after Na had been introduced into
360 the inclusion (Simon et al., 2005), gave rise to Na-bearing, reversely zoned melilite,
361 indicating a much slower cooling rate (MacPherson et al., 1984). The sharply contrasting
362 inferred cooling rates for the two events that affected Golfball suggest that the formation
363 of CAIs did not occur by a unique heating mechanism but by multiple heating
364 mechanisms in the early Solar System.

365 **4.2 Short time interval between precursor formation and partial melting event**

366 During the first partial melting event, spinel was also the liquidus phase.
367 Nevertheless, all the Al–Mg isotope data, which include both the relict and overgrowth
368 minerals, plot on a well-defined, single isochron with $(^{26}\text{Al}/^{27}\text{Al})_0 = (4.42 \pm 0.20) \times 10^{-5}$
369 and $(\delta^{26}\text{Mg}^*)_0 = -0.035 \pm 0.050\text{‰}$ (Fig. 8). The Al–Mg system of the Al-rich relict grains
370 might have been reset during the partial melting event by Mg self-diffusion associated
371 with Mg-isotope exchange with the melt, resulting in the single isochron. According to
372 the timescale required to keep the O-isotope gradient in the melt discussed above, a
373 diffusion distance of Mg-isotopes in the Al-rich melilite grains during the partial melting
374 is calculated to be less than $0.03 \mu\text{m}$, using Mg self-diffusion coefficients in gehlenite (Ito

375 and Ganguly, 2009). Furthermore, the transition zones show steep gradients of åkermanite
376 contents over $\sim 1 \mu\text{m}$ (Figs. 4c and 4d). Therefore, the interdiffusion distances of Al + Al
377 vs. Mg + Si during the partial melting should be less than $1 \mu\text{m}$ if it occurred. At the
378 temperatures between 1230 and 1400°C, interdiffusion coefficients of Al + Al vs. Mg +
379 Si for gehlenitic melilite (Nagasawa et al., 2001) and the Mg self-diffusion coefficients
380 for gehlenite are comparable to each other. Thus, the Mg self-diffusion distance in the Al-
381 rich relict grains during the partial melting event should be less than $\sim 1 \mu\text{m}$, which is
382 much smaller than the sizes of Al-rich relict grains. These two independent estimations
383 of Mg-isotope mobility indicate that the Al–Mg system of the Al-rich relict grains have
384 effectively been kept in a closed system during the partial melting event. The well-defined
385 mineral isochron suggests that the partial melting event occurred in very short order after
386 precursor formation. Based on analytical errors of $(^{26}\text{Al}/^{27}\text{Al})_0$, the time gap between the
387 precursor formation and the partial melting event is shorter than 0.09 Myr.

388 **4.3 Precursor of Golfball**

389 If Al/Mg chemical fractionation for Golfball occurred at the formation time of
390 “canonical” CAIs with $(^{26}\text{Al}/^{27}\text{Al})_0 = \sim 5.2 \times 10^{-5}$ (Jacobsen et al., 2008; Larsen et al.,
391 2011), the Mg-isotopic composition of Golfball would have evolved with the bulk
392 $^{27}\text{Al}/^{24}\text{Mg}$ of 2.4 (Simon and Grossman, 2004) on an evolution curve shown as the green-
393 colored area in the Mg-isotope evolution diagram of Fig. 10, to have $(\delta^{26}\text{Mg}^*)_0 = 0.10 \pm$
394 0.05‰ at $^{26}\text{Al}/^{27}\text{Al} = (4.42 \pm 0.20) \times 10^{-5}$. However, the inferred $(\delta^{26}\text{Mg}^*)_0$ of $-0.035 \pm$
395 0.050‰ is clearly lower than that evolved value, suggesting Golfball is not an object
396 formed by remelting of canonical CAIs formed when $^{26}\text{Al}/^{27}\text{Al} = \sim 5.2 \times 10^{-5}$.

397 Instead, on the Mg-isotope evolution diagram (Fig. 10), the initial values of
398 Golfball plot on the Mg-isotope evolution curve of solar-composition gas. Initial values,

399 $(^{26}\text{Al}/^{27}\text{Al})_0$ and $(\delta^{26}\text{Mg}^*)_0$, for FTAs and FGIs also all plot on the Mg-isotope evolution
400 curve of solar-composition gas, despite their significant variations in $(^{26}\text{Al}/^{27}\text{Al})_0$ from
401 ~ 5.2 to $\sim 3.4 \times 10^{-5}$ (Fig. 10). This consistency of initial values for Golfball with those for
402 the FTAs and FGIs implies that precursor materials of Golfball contained FTAs and/or
403 FGIs. The presence of Al-rich melilite with $< \text{Åk}_{15}$ is very common in FTAs and FGIs
404 from the CV chondrites (e.g., MacPherson and Grossman, 1984; Katayama et al., 2012;
405 Kawasaki et al., 2020; Wada et al., 2020) and O-isotopic compositions of their melilite
406 crystals have been reported to exhibit disequilibrium distributions along the CCAM line
407 between $\Delta^{17}\text{O} \sim -23\text{‰}$ and 1‰ (e.g., Katayama et al., 2012; Kawasaki et al., 2012, Wada
408 et al., 2020), which covers the range of O-isotopic variations ($\Delta^{17}\text{O} \sim -14\text{‰}$ to -5‰)
409 observed for the blocky melilite crystals in the Golfball core. This consistency of O-
410 isotopic compositions supports the above conclusion that the O-isotopic variations of the
411 blocky melilite crystals indicate inheritance of the O-isotope heterogeneity of precursor
412 materials. Furthermore, the $\delta^{25}\text{Mg}$ values of Al-rich relict melilite grains, averaging $1.4 \pm$
413 1.5‰ , are consistent with ranges of those for melilite in FTAs (MacPherson et al., 2012;
414 Kawasaki et al., 2017, 2019) and FGIs (MacPherson et al., 2010; Kawasaki et al., 2020).
415 These chemical and O and Mg-isotopic signatures all suggest that the precursor of
416 Golfball contained FTAs and/or FGIs. The partial melting events affecting Golfball may
417 have occurred in very short order after the formation of precursor FTAs and/or FGIs.

418 The formation event of Golfball occurred at 0.18 ± 0.05 Myr after the formation
419 of canonical CAIs (Jacobsen et al., 2008; Larsen et al., 2011), under the assumption of
420 homogeneous distributions of ^{26}Al in the forming region. The remelting of Golfball CAI
421 is consistent with the conclusion that CAI-formation thermal processes of condensation
422 and melting occurred contemporaneously during ~ 0.4 Myr at the very beginning of the

423 Solar System (Kawasaki et al., 2020).

424

425

5. CONCLUSIONS

426 *In situ* O-isotope analysis and Al–Mg systematics of the Allende Type B CAI Golfball
427 provide constraints on the cooling rate, age, and precursor materials of the CAI. Many of
428 the blocky melilite crystals in the core of Golfball contain Al-rich relict grains that are
429 enclosed in strongly zoned overgrowths. The O-isotopic compositions of the blocky
430 melilite crystals range between $\Delta^{17}\text{O} \sim -14\text{‰}$ and -5‰ . The Al-rich relict melilite grains
431 and their overgrowths exhibit the same O-isotopic compositions, while the O-isotopic
432 compositions are varied spatially among melilites. We found an area in which O-isotopic
433 compositions gradually change across several melilite crystals over a distance of $\sim 21 \mu\text{m}$.
434 The O-isotopic compositions of the melt could not have been homogenized during the
435 partial melting event in that scale and thus O-isotope exchange with the nebular gas was
436 insufficient in the Golfball melt if it occurred. Using the O self-diffusion coefficient in
437 the melt, a cooling rate following partial melting is calculated to be $6 \times 10^4 \text{ K/h}$ or more.
438 The Golfball experienced an extremely short heating event, differing from heating of
439 typical Type B CAIs. The Al–Mg isotope data, including the relict and overgrown
440 minerals, plot on the well-defined single mineral isochron with initial values of
441 $(^{26}\text{Al}/^{27}\text{Al})_0 = (4.42 \pm 0.20) \times 10^{-5}$ and $(\delta^{26}\text{Mg}^*)_0 = -0.035 \pm 0.050\text{‰}$. The consistency of
442 the initial values and chemical and O-isotopic compositions of melilite with those for
443 FTAs and FGIs implies that precursor materials of Golfball contained FTAs and/or FGIs.
444 The partial melting events for Golfball may have occurred in very short order after the
445 formation of precursor FTAs and/or FGIs, supporting the contemporaneous formation of
446 condensate CAIs and igneous CAIs.

447

448

ACKNOWLEDGMENTS

449 This article is dedicated to Prof. John T. Wasson in honor of his outstanding contributions
450 to cosmochemistry. We thank Andrew M. Davis and an anonymous reviewer for their
451 constructive comments and the Associate Editor Yves Marrocchi for his editorial efforts.
452 We thank Kosuke Nagata for technical assistance. This work is partly supported by
453 Monka-sho grants.

454

455

REFERENCES

- 456 Aléon J., El Goresy A. and Zinner E. (2007) Oxygen isotope heterogeneities in the earliest
457 protosolar gas recorded in a meteoritic calcium–aluminum-rich inclusion. *Earth
458 and Planetary Science Letters* **263**, 114–127.
- 459 Aléon J. (2016) Oxygen isotopes in the early protoplanetary disk inferred from pyroxene
460 in a classical type B CAI. *Earth and Planetary Science Letters* **440**, 62–70.
- 461 Aléon J. (2018) Closed system oxygen isotope redistribution in igneous CAIs upon spinel
462 dissolution. *Earth and Planetary Science Letters* **482**, 324–333.
- 463 Beckett J. R., Paque J. M. and Stolper E. (1999) The use of melilite compositions to
464 constrain the thermal history and liquid line of descent of type B CAIs. *Lunar
465 Planetary Science Conference* **30**, #1920.
- 466 Beckett J. R., Simon S. B. and Stolper E. (2000) The partitioning of Na between melilite
467 and liquid: Part II. Applications to Type B inclusions from carbonaceous
468 chondrites. *Geochimica et Cosmochimica Acta* **64**, 2519–2534.

469 Catanzaro, E. J., Murphy, T. J., Garner, E. L. and Shields, W. R. (1966) Absolute isotopic
470 abundance ratios and atomic weights of magnesium. *J. Res. natl. Bur Stand.* **70a**,
471 453-458.

472 Clayton R. N., Onuma N., Grossman L. and Mayeda T. K. (1977) Distribution of the
473 presolar component in Allende and other carbonaceous chondrites. *Earth and*
474 *Planetary Science Letters* **34**, 209–224.

475 Clayton R. N. (1993) Oxygen isotopes in meteorites. *Annual Review of Earth and*
476 *Planetary Sciences* **21**, 115–149.

477 Connelly J. N., Bizzarro M., Krot A. N., Nordlund Å., Wielandt D. and Ivanova M. A.
478 (2012) The absolute chronology and thermal processing of solids in the solar
479 protoplanetary disk. *Science* **338**, 651–655.

480 Galy A., Yoffe O., Janney P. E., Williams R. W., Cloquet C., Alard O., Halicz L., Wadhwa
481 M., Hutcheon I. D., Ramon E. and Carignan J. (2003) Magnesium isotope
482 heterogeneity of the isotopic standard SRM980 and new reference materials for
483 magnesium-isotope-ratio measurements. *Journal of Analytical Atomic*
484 *Spectrometry.* **18**, 1352–1356.

485 Grossman L., Simon S. B., Rai V. K., Thiemens M. H., Hutcheon I. D., Williams R. W.,
486 Galy A., Ding T., Fedkin A. V., Clayton R. N. and Mayeda T. K. (2008) Primordial
487 compositions of refractory inclusions. *Geochimica et Cosmochimica Acta* **72**,
488 3001–3021.

489 Davis A. M., Richter F. M., Mendybaev R. A., Janney P. E., Wadhwa M. and McKeegan
490 K. D. (2015) Isotopic mass fractionation laws for magnesium and their effects on
491 ^{26}Al – ^{26}Mg systematics in solar system materials. *Geochimica et Cosmochimica*
492 *Acta* **158**, 245–261.

493 Holst J. C., Olsen M. B., Paton C., Nagashima K., Schiller M., Wielandt D., Larsen K. K.,
494 Connelly J. N., Jorgensen J. K., Krot A. N., Nordlund A. and Bizzarro M. (2013)
495 ^{182}Hf - ^{182}W age dating of a ^{26}Al -poor inclusion and implications for the origin of
496 short-lived radioisotopes in the early Solar System. *Proceedings of the National*
497 *Academy of Sciences of the United States of America* **110**, 8819–8823.

498 Hsu W., Wasserburg G. J. and Huss G. R. (2000). High time resolution by use of the ^{26}Al
499 chronometer in the multistage formation of a CAI. *Earth and Planetary Science*
500 *Letters* **182**, 15–29.

501 Ito, M., Nagasawa, H. and Yurimoto, H. (2004) Oxygen isotopic SIMS analysis in Allende
502 CAI: details of the very early thermal history of the solar system. *Geochimica et*
503 *Cosmochimica Acta* **68**, 2905–2923.

504 Ito M., Nagasawa H. and Yurimoto H. (2006) A study of Mg and K isotopes in Allende
505 CAIs: Implications to the time scale for the multiple heating processes.
506 *Meteoritics & Planetary Science* **41**, 1871–1881.

507 Ito M. and Ganguly J. (2009) Magnesium diffusion in minerals in CAIs: new
508 experimental data for melilites and implications for the Al-Mg chronometer and
509 thermal history of CAIs. *Lunar Planetary Science Conference* **40**, #1753.

510 Itoh S., Makide K. and Yurimoto H. (2008) Calculation of radiogenic ^{26}Mg of CAI
511 minerals under high precision isotope measurement by SIMS. *Applied Surface*
512 *Science* **255**, 1476–1478.

513 Itoh S., Simon S. B., Grossman L. and Yurimoto H. (2009) Al-Mg isochron study
514 combined with oxygen isotope analysis of the Allende type B CAI, Golfball.
515 (abstract #5307) 72nd Annual Meteoritical Society Meeting.

516 Jacobsen B., Yin Q., Moynier F., Amelin Y., Krot A. N., Nagashima K., Hutcheon I. D.

517 and Palme H. (2008) ^{26}Al - ^{26}Mg and ^{207}Pb - ^{206}Pb systematics of Allende CAIs:
518 Canonical solar initial $^{26}\text{Al}/^{27}\text{Al}$ ratio reinstated. *Earth and Planetary Science*
519 *Letters* **272**, 353–364.

520 Jones R. H., Villeneuve J. and Libourel G. (2018) Thermal histories of chondrules:
521 Petrologic observations and experimental constraints. In *Chondrules: Records of*
522 *Protoplanetary Disk Processes* (ed. S. S. Russell, H. C. Connolly Jr. and A. N.
523 Krot), pp. 57–90. Cambridge University Press.

524 Katayama J., Itoh S. and Yurimoto H. (2012) Oxygen isotopic zoning of reversely zoned
525 melilite crystals in a Fluffy Type A Ca-Al-rich inclusion from the Vigarano
526 meteorite. *Meteoritics & Planetary Science* **47**, 2094–2106.

527 Kawasaki N., Sakamoto N. and Yurimoto H. (2012) Oxygen isotopic and chemical zoning
528 of melilite crystals in a Type A Ca-Al-rich inclusion of Efremovka CV3 chondrite.
529 *Meteoritics & Planetary Science* **47**, 2084–2093.

530 Kawasaki, N., Kato, C., Itoh, S., Wakaki, S., Ito, M. and Yurimoto, H. (2015) ^{26}Al - ^{26}Mg
531 chronology and oxygen isotope distributions of multiple melting for a Type C CAI
532 from Allende. *Geochimica et Cosmochimica Acta* **169**, 99–114.

533 Kawasaki N., Itoh S., Sakamoto N. and Yurimoto H. (2017) Chronological study of
534 oxygen isotope composition for the solar protoplanetary disk recorded in a fluffy
535 Type A CAI from Vigarano. *Geochimica et Cosmochimica Acta* **201**, 83–102.

536 Kawasaki N., Simon S. B., Grossman L., Sakamoto N. and Yurimoto H. (2018) Crystal
537 growth and disequilibrium distribution of oxygen isotopes in an igneous Ca-Al-
538 rich inclusion from the Allende carbonaceous chondrite. *Geochimica et*
539 *Cosmochimica Acta* **221**, 318–341.

540 Kawasaki N., Park C., Sakamoto N., Park S. Y., Kim H. N., Kuroda M. and Yurimoto H.

541 (2019) Variations in initial $^{26}\text{Al}/^{27}\text{Al}$ ratios among fluffy Type A Ca–Al-rich
542 inclusions from reduced CV chondrites. *Earth and Planetary Science Letters* **511**,
543 25–35.

544 Kawasaki N., Wada S., Park C., Sakamoto N. and Yurimoto H. (2020) Variations in initial
545 $^{26}\text{Al}/^{27}\text{Al}$ ratios among fine-grained Ca–Al-rich inclusions from reduced CV
546 chondrites. *Geochimica et Cosmochimica Acta* **279**, 1–15.

547 Kita N. T., Ushikubo T., Knight K. B., Mendybaev R. A., Davis A. M., Richter F. M. and
548 Fournelle J. H. (2012) Internal ^{26}Al - ^{26}Mg isotope systematics of a Type B CAI:
549 Remelting of refractory precursor solids. *Geochimica et Cosmochimica Acta* **86**,
550 37–51.

551 Kööp L., Davis A. M., Nakashima D., Park C., Krot A. N., Nagashima K., Tenner T. J.,
552 Heck P. R. and Kita N. T. (2016) A link between oxygen, calcium and titanium
553 isotopes in ^{26}Al -poor hibonite-rich CAIs from Murchison and implications for the
554 heterogeneity of dust reservoirs in the solar nebula. *Geochimica et Cosmochimica*
555 *Acta* **189**, 70–95.

556 Krot A. N., Yurimoto H., Hutcheon I. D. and MacPherson G. J. (2005) Chronology of the
557 early Solar System from chondrule-bearing calcium-aluminium-rich inclusions.
558 *Nature* **434**, 998–1001.

559 Krot A. N., Yurimoto H., Hutcheon I. D., Chaussidon M., MacPherson G. J. and Paque J.
560 (2007) Remelting of refractory inclusions in the chondrule-forming regions:
561 Evidence from chondrule-bearing type C calcium-aluminum-rich inclusions from
562 Allende. *Meteoritics & Planetary Science* **42**, 1197–1219.

563 Krot A. N., Chaussidon M., Yurimoto H., Sakamoto N., Nagashima K., Hutcheon I. D.
564 and MacPherson G. J. (2008a) Oxygen isotopic compositions of Allende Type C

565 CAIs: Evidence for isotopic exchange during nebular melting and asteroidal
566 metamorphism. *Geochimica et Cosmochimica Acta* **72**, 2534–2555.

567 Krot A. N., Nagashima K., Bizzarro M., Huss G. R., Davis A. M., McKeegan K. D.,
568 Meyer B. S. and Ulyanov A. A. (2008b) Multiple generations of refractory
569 inclusions in the metal-rich carbonaceous chondrites Acfer 182/214 and Isheyevu.
570 *The Astrophysical Journal* **672**, 713–721.

571 Larsen K. K., Trinquier A., Paton C., Schiller M., Wielandt D., Ivanova M. A., Connelly
572 J. N., Nordlund Å., Krot A. N. and Bizzarro M. (2011) Evidence for magnesium
573 isotope heterogeneity in the solar protoplanetary disk. *The Astrophysical Journal*
574 *Letters* **735**, L37–L43.

575 Larsen K. K., Wielandt D., Schiller M., Krot A. N. and Bizzarro M. (2020) Episodic
576 formation of refractory inclusions in the Solar System and their presolar heritage.
577 *Earth and Planetary Science Letters* **535**, 116088.

578 Lasaga A. C. (1983) Geospeedometry: an extension of geothermometry. In *Kinetics and*
579 *Equilibrium in Mineral Reactions* (ed. S. K. Saxena), pp. 81–114, Springer-Verlag,
580 New York.

581 Leshner C. E., Hervig R. L. and Tinker D. (1996) Self diffusion of network formers (silicon
582 and oxygen) in naturally occurring basaltic liquid. *Geochimica et Cosmochimica*
583 *Acta* **60**, 405–413.

584 Lee T., Papanastassiou D. A. and Wasserburg G. J. (1976) Demonstration of ^{26}Mg excess
585 in Allende and evidence for ^{26}Al . *Geophysical Research Letters* **3**, 41–44.

586 Lodders K. (2003) Solar system abundances and condensation temperatures of the
587 elements. *The Astrophysical Journal* **591**, 1220–1247.

588 Ludwig K. (2003) ISOPLOT: A Geochronological Toolkit for Microsoft Excel 3.00.

589 Berkeley Geochronological Center Special Publication No. 4, Berkeley, CA 94709.

590 MacPherson G. J. and Grossman L. (1981) A once-molten, coarse-grained, Ca-rich
591 inclusion in Allende. *Earth and Planetary Science Letters* **52**, 16–24.

592 MacPherson G. J. and Grossman L. (1984) Fluffy Type A Ca-, Al-rich inclusions in the
593 Allende meteorite. *Geochimica et Cosmochimica Acta* **48**, 29–46.

594 MacPherson G. J., Paque J. M., Stolper E. and Grossman L. (1984) The origin and
595 significance of reverse zoning in melilite from Allende Type B inclusions. *The*
596 *Journal of Geology* **92**, 289–305.

597 MacPherson G. J. and Davis A. M. (1993) A petrologic and ion microprobe study of a
598 Vigarano Type B refractory inclusions: Evolution by multiple stages of alteration
599 and melting. *Geochimica et Cosmochimica Acta* **57**, 231–243.

600 MacPherson G. J., Davis A. M. and Zinner E. K. (1995) The distribution of aluminum-26
601 in the early Solar System-A reappraisal. *Meteoritics* **30**, 365–386.

602 MacPherson G. J., Bullock E. S., Janney P. E., Kita N. T., Ushikubo T., Davis A. M.,
603 Wadhwa M. and Krot A. N. (2010) Early solar nebular condensates with canonical,
604 not supracanonical, initial $^{26}\text{Al}/^{27}\text{Al}$ ratios. *The Astrophysical Journal Letters* **711**,
605 L117–L121.

606 MacPherson G. J., Kita N. T., Ushikubo T., Bullock E. S. and Davis A. M. (2012) Well-
607 resolved variations in the formation ages for Ca-Al-rich inclusions in the early
608 Solar System. *Earth and Planetary Science Letters* **331–332**, 43–54.

609 MacPherson G. J., Bullock E. S., Tenner T. J., Nakashima D., Kita N. T., Ivanova M. A.,
610 Krot A. N., Petaev M. I. and Jacobsen S. B. (2017) High precision Al–Mg
611 systematics of forsterite-bearing Type B CAIs from CV3 chondrites. *Geochimica*
612 *et Cosmochimica Acta* **201**, 65–82.

- 613 MacPherson G. J., Defouilloy C. and Kita N. T. (2018) High-precision Al–Mg isotopic
614 systematics in USNM 3898 – The benchmark “ALL” for initial $^{87}\text{Sr}/^{86}\text{Sr}$ in the
615 earliest Solar System. *Earth and Planetary Science Letters* **491**, 238–243.
- 616 Makide K., Nagashima K., Krot A. N., Huss G. R., Ciesla F. J., Hellebrand E., Gaidos E.
617 and Yang L. (2011) Heterogeneous distribution of ^{26}Al at the birth of the solar
618 system. *The Astrophysical Journal Letters* **733**, L31–L34.
- 619 Matsuda N., Sakamoto N., Tachibana S. and Yurimoto H. (2019) Heating duration of
620 igneous rim formation on a chondrule in the Northwest Africa 3118 CV3_{oxA}
621 carbonaceous chondrite inferred from micro-scale migration of the oxygen
622 isotopes. *Geochemistry* **79**, 125524.
- 623 Nagasawa H., Suzuki T., Ito M. and Morioka M. (2001) Diffusion in single crystal of
624 melilite: interdiffusion of Al + Al vs. Mg + Si. *Physics and Chemistry of Minerals*
625 **28**, 706–710.
- 626 Norris T. L., Gancarz A. J., Rokop D. J. and Thomas K. W. (1983) Half-life of ^{26}Al .
627 *Journal of Geophysical Research* **88**, B331–B333.
- 628 Park C., Wakaki S., Sakamoto N., Kobayashi S. and Yurimoto H. (2012) Oxygen isotopic
629 variations of melilite crystals in a Type A CAI from Allende. *Meteoritics &*
630 *Planetary Science* **47**, 2070–2083.
- 631 Park C., Nagashima K., Krot A. N., Huss G. R., Davis A. M. and Bizzarro M. (2017)
632 Calcium-aluminum-rich inclusions with fractionation and unidentified nuclear
633 effects (FUN CAIs): II. Heterogeneities of magnesium isotopes and ^{26}Al in the
634 early Solar System inferred from in situ high-precision magnesium-isotope
635 measurements. *Geochimica et Cosmochimica Acta* **201**, 6–24.
- 636 Podosek F. A., Zinner E. K., MacPherson G. J., Lundberg L. L. Brannon J. C. and Fahey

637 A. J. (1991) Correlated study of initial $^{87}\text{Sr}/^{86}\text{Sr}$ and Al-Mg isotopic systematics
638 and petrologic properties in a suite of refractory inclusions from the Allende
639 meteorite. *Geochimica et Cosmochimica Acta* **55**, 1083–1110.

640 Shewmon P. (1963) *Diffusion in Solids*, McGraw-Hill, New York.

641 Simon S. B., Davis A. M. and Grossman L. (1999) Origin of compact type A refractory
642 inclusions from CV3 carbonaceous chondrites. *Geochimica et Cosmochimica*
643 *Acta* **63**, 1233–1248.

644 Simon S. B. and Grossman L. (2004) A preferred method for the determination of bulk
645 compositions of coarse-grained refractory inclusions and some implications of the
646 results. *Geochimica et Cosmochimica Acta* **68**, 4237–4248.

647 Simon S. B., Grossman L. and Davis A. M. (2005) A unique type B inclusion from
648 Allende with evidence for multiple stages of melting. *Meteoritics & Planetary*
649 *Science* **40**, 461–475.

650 Stolper E. and Paque J. M. (1986) Crystallization sequences of Ca-Al-rich inclusions
651 from Allende: The effects of cooling rate and maximum temperature. *Geochimica*
652 *et Cosmochimica Acta* **50**, 1785–1806.

653 Wada S., Kawasaki N., Park C. and Yurimoto H. (2020) Melilite condensed from an ^{16}O -
654 poor gaseous reservoir: Evidence from a fine-grained Ca-Al-rich inclusion of
655 Northwest Africa 8613. *Geochimica et Cosmochimica Acta* **288**, 161–175.

656 Wakaki S., Itoh S., Tanaka T. and Yurimoto H. (2013) Petrology, trace element
657 abundances and oxygen isotopic compositions of a compound CAI-chondrule
658 object from Allende. *Geochimica et Cosmochimica Acta* **102**, 261–279.

659 Wark D. A. and Lovering J. F. (1982) The nature and origin of type B1 and B2 Ca-Al-rich
660 inclusions in the Allende meteorite. *Geochimica et Cosmochimica Acta* **46**, 2581–

661 2594.

662 Wark D. A. (1987) Plagioclase-rich inclusions in carbonaceous chondrite meteorites:
663 liquid condensates? *Geochimica et Cosmochimica Acta* **51**, 221–242.

664 Wasserburg G. J., Lee T. and Papanastassiou D. A. (1977) Correlated O and Mg isotopic
665 anomalies in Allende inclusions: II. Magnesium. *Geophysical Research Letters* **4**,
666 299–302.

667 Yamamoto D., Tachibana S., Kawasaki N., Kamibayashi M. and Yurimoto H. (2019)
668 Oxygen isotope exchange between CAI melt and water vapor: An experimental
669 study. (abstract #2157) 82nd Annual Meteoritical Society Meeting.

670 Yoshitake M., Koide Y. and Yurimoto H. (2005) Correlations between oxygen-isotopic
671 composition and petrologic setting in a coarse-grained Ca, Al-rich inclusion.
672 *Geochimica et Cosmochimica Acta* **69**, 2663–2674.

673 Yurimoto H., Nagasawa H., Mori Y. and Matsubaya O. (1994) Micro-distribution of
674 oxygen isotopes in a refractory inclusion from the Allende meteorite. *Earth and*
675 *Planetary Science Letters* **128**, 47–53.

676 Yurimoto H., Ito M. and Nagasawa H. (1998) Oxygen isotope exchange between
677 refractory inclusion in Allende and solar nebula gas. *Science* **282**, 1874–1877.

678 Yurimoto H. and Wasson J. T. (2002) Extremely rapid cooling of a carbonaceous-
679 chondrite chondrule containing very ¹⁶O-rich olivine and a ²⁶Mg-excess.
680 *Geochimica et Cosmochimica Acta* **66**, 4355–4363.

681 Yurimoto H., Nagashima K. and Kunihiro T. (2003) High precision isotope micro-
682 imaging of materials. *Applied Surface Science* **203–204**, 793–797.

683

684 Table 1. Average O-isotopic compositions (‰) of spinel in the core of Golfball.

Occurrence	No. of analyses	$\delta^{17}\text{O}$	2σ	$\delta^{18}\text{O}$	2σ	$\Delta^{17}\text{O}$	2σ
<i>Core, framboïd</i>	20	-47.9	1.9	-45.9	1.1	-24.1	1.8
<i>Core, in fassaïte</i>	7	-48.1	2.0	-46.3	0.9	-24.1	1.9
<i>Core, in lath melilite</i>	8	-47.5	1.7	-45.8	1.1	-23.7	2.1
Average	35	-47.9	1.9	-45.9	1.1	-24.0	1.9

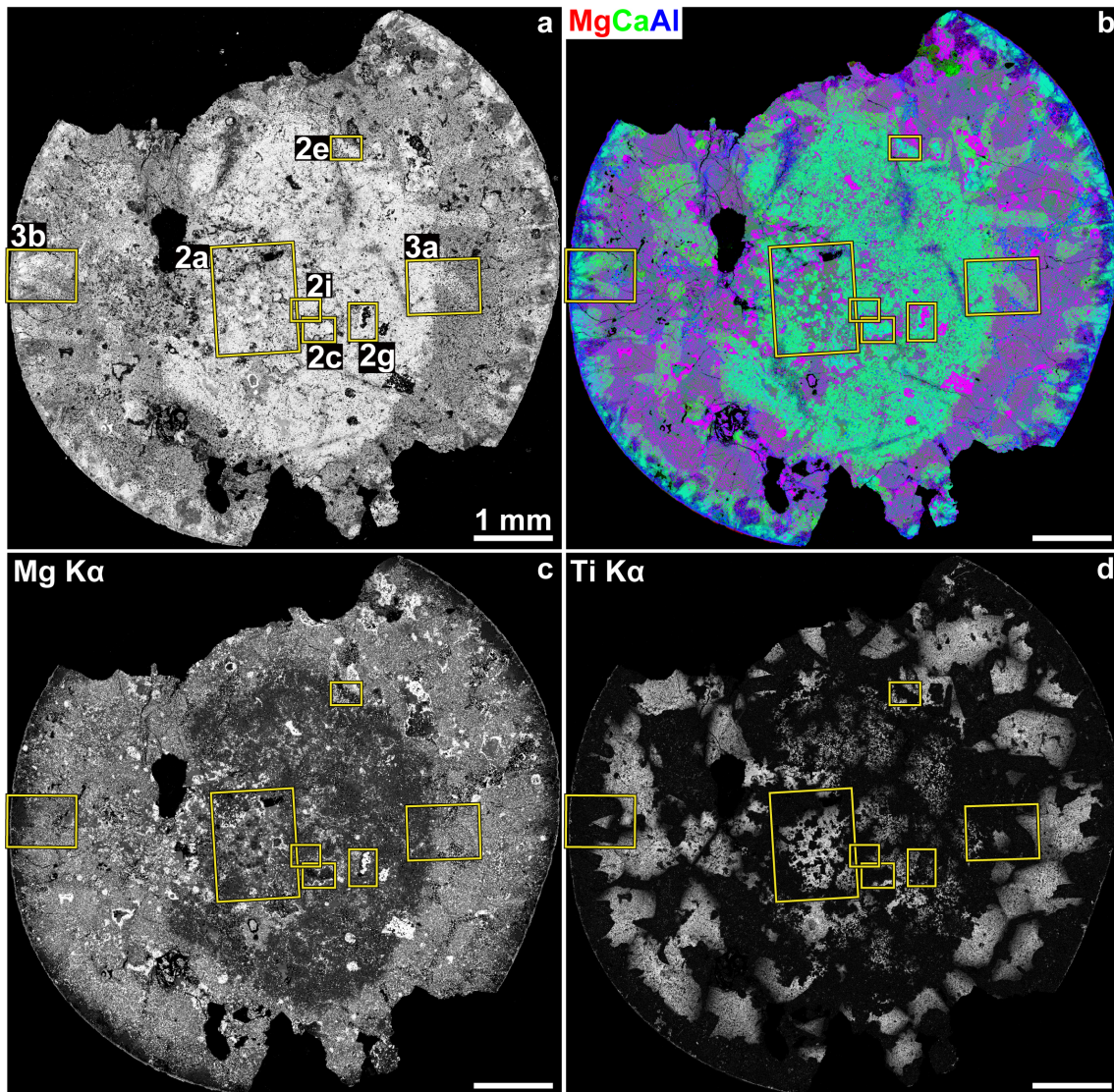
685 Bold data: average values of all measurements for spinel

686

687 Table 2. Mg-isotopic compositions (‰) and $^{27}\text{Al}/^{24}\text{Mg}$ ratios of minerals in the core of
 688 Golfball.

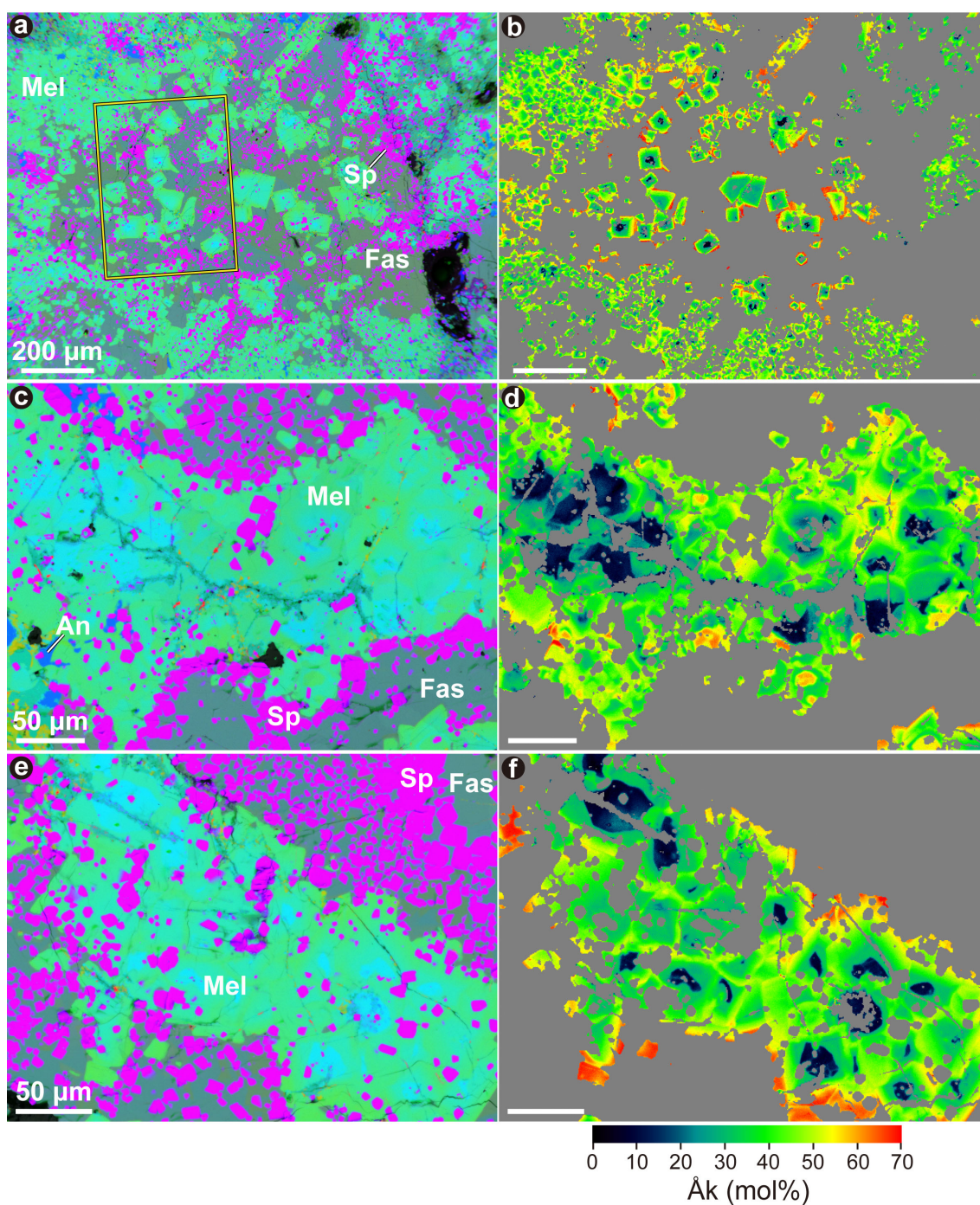
Spot #	$^{27}\text{Al}/^{24}\text{Mg}$	2σ	$\delta^{26}\text{Mg}^*$	2σ	$\delta^{25}\text{Mg}$	2σ
<i>Melilite, core, blocky, Al-rich grains</i>						
5	16.1	0.1	4.9	1.3	1.0	1.1
6	20.4	0.1	7.2	1.3	0.2	1.0
8	16.6	0.1	5.3	1.3	1.1	1.0
9	24.3	0.1	7.4	1.2	1.7	1.1
183	23.7	0.6	6.9	1.7	1.4	1.5
184	24.0	0.4	7.7	1.2	0.3	1.4
185	25.1	0.4	8.2	1.2	1.2	1.4
187	27.4	0.4	9.4	1.2	1.7	1.4
189	20.3	0.3	6.2	1.2	1.8	1.4
191	42.2	1.1	13.3	1.2	2.2	1.5
192	25.9	0.6	7.5	1.3	2.7	1.4
193	17.0	0.2	5.0	1.1	1.9	1.4
<i>Melilite, core, blocky, overgrown grains</i>						
229	5.00	0.01	1.51	0.13	1.73	0.09
311	6.10	0.08	1.92	0.12	1.80	0.05
312	4.80	0.03	1.51	0.13	1.93	0.05
<i>Spinel, core, framboid</i>						
351	2.480	0.001	0.73	0.08	1.80	0.06
352	2.484	0.005	0.82	0.08	1.75	0.04
353	2.497	0.004	0.74	0.07	1.85	0.04
365	2.487	0.004	0.72	0.07	1.84	0.04
367	2.498	0.004	0.81	0.08	1.68	0.05
<i>Spinel, core, in melilite</i>						
347	2.484	0.006	0.73	0.07	1.82	0.03

690



691

692 Figure 1. (a) Backscattered electron (BSE) image of an Allende Type B CAI Golfball,
 693 section GBL2. Yellow boxes indicate the areas shown in Figs. 2 and 3. (b) Combined X-
 694 ray elemental map with Mg (red), Ca (green), and Al (blue), (c) Mg $K\alpha$ elemental map,
 695 and (d) Ti $K\alpha$ elemental map of the same field of view. Melilite at the outermost edge of
 696 the inclusion appears white in (a) and blue in (b). The melilite core appears white in (a)
 697 and green in (b). The spinel-fassaite mantle is gray in (a) and purple in (b). Note melilite
 698 laths extending from the core into the mantle, visible in (a) and (b).

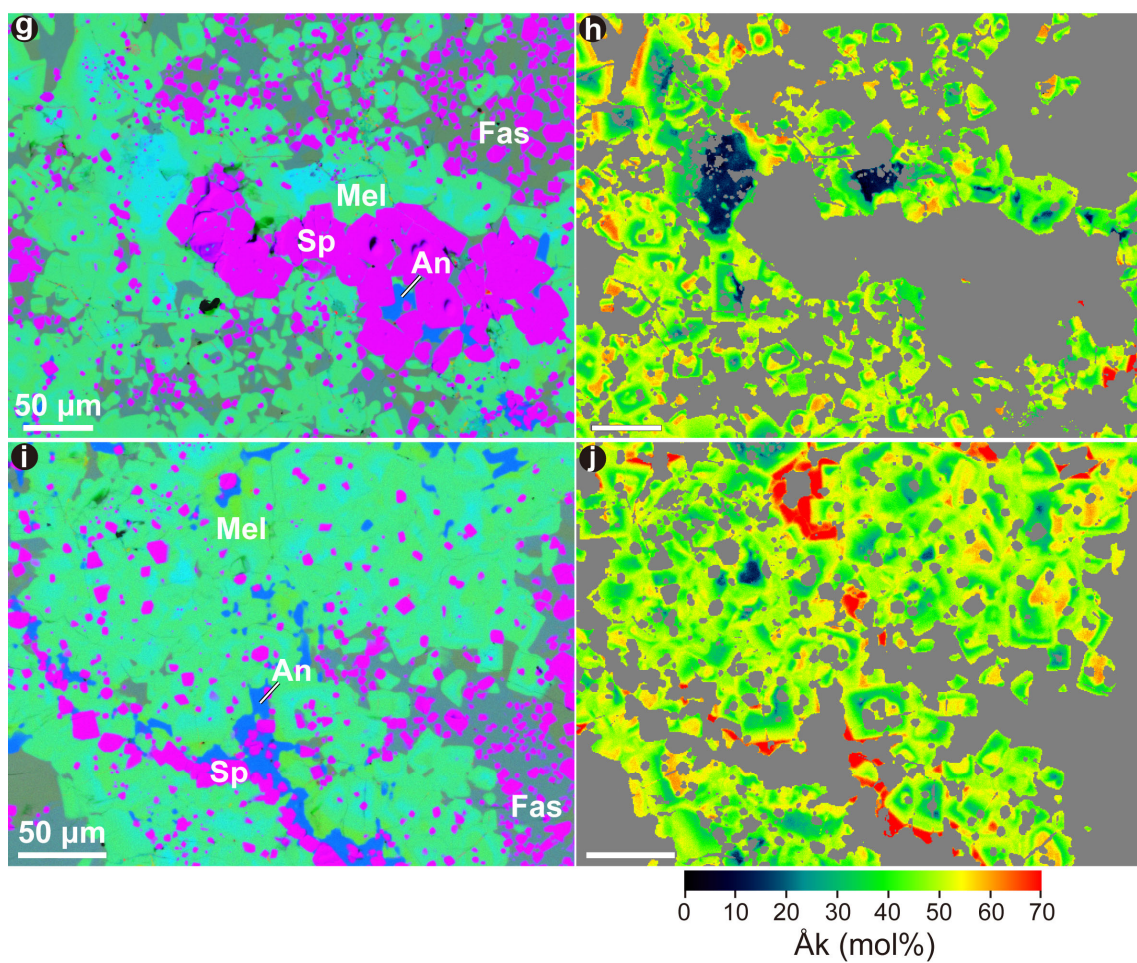


699

700 Figure 2. Combined X-ray elemental map of areas indicated in Fig. 1, showing Mg (red),
 701 Ca (green), and Al (blue) and corresponding quantitative map of åkermanite content (Åk)
 702 in melilite from the same areas. Mineral phases except melilite and cracks are masked in
 703 gray. (a,b) area 1; (c,d) area 2; (e,f) area 3; (g,h) area 4; (i,j) area 5. Areas 1 and 4 are
 704 rotated ~90 degrees from the view in Fig. 1. An, anorthite; Fas, fassaite; Mel, melilite; Sp,

705 spinel.

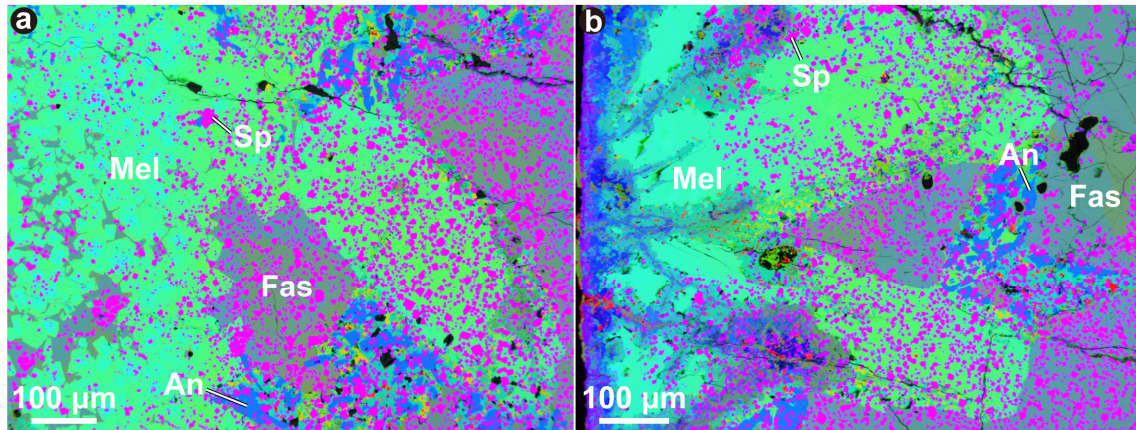
706



707

708 Figure 2 (*continued*)

709



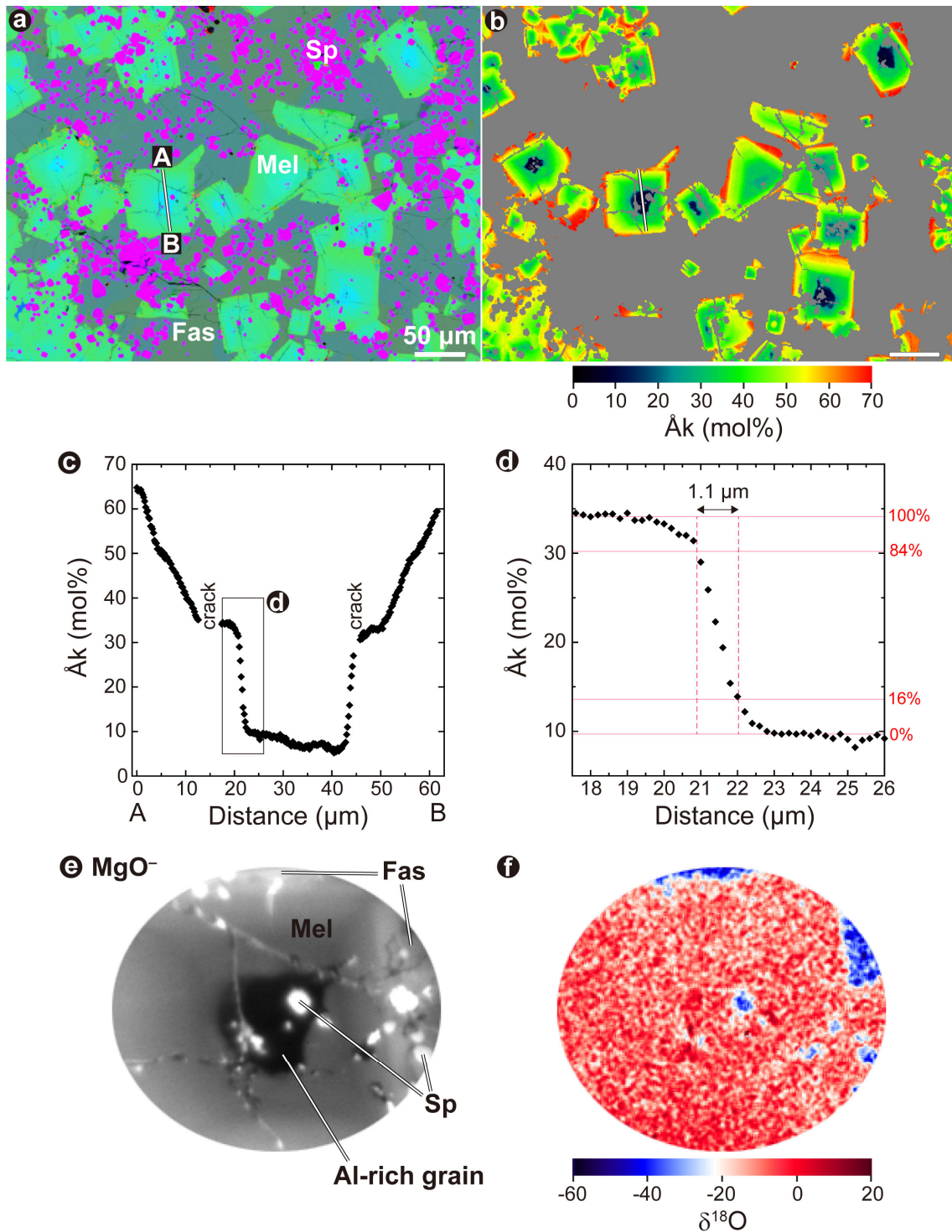
710

711 Figure 3. Combined X-ray elemental map of areas indicated in Fig. 1, showing Mg (red),

712 Ca (green), and Al (blue). An, anorthite; Fas, fassaite; Mel, melilite; Sp, spinel. BSE

713 images of the same areas are shown in Supplementary materials.

714



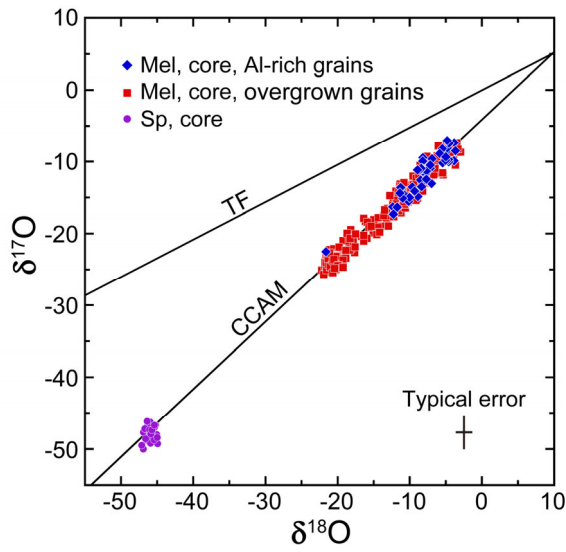
715

716 Figure 4. (a) Combined X-ray elemental map of an area indicated by yellow box in Fig.

717 2a, showing Mg (red), Ca (green), and Al (blue). (b) Quantitative map of åkermanite

718 content (Åk) in melilite shown in (a). Mineral phases except melilite and cracks are

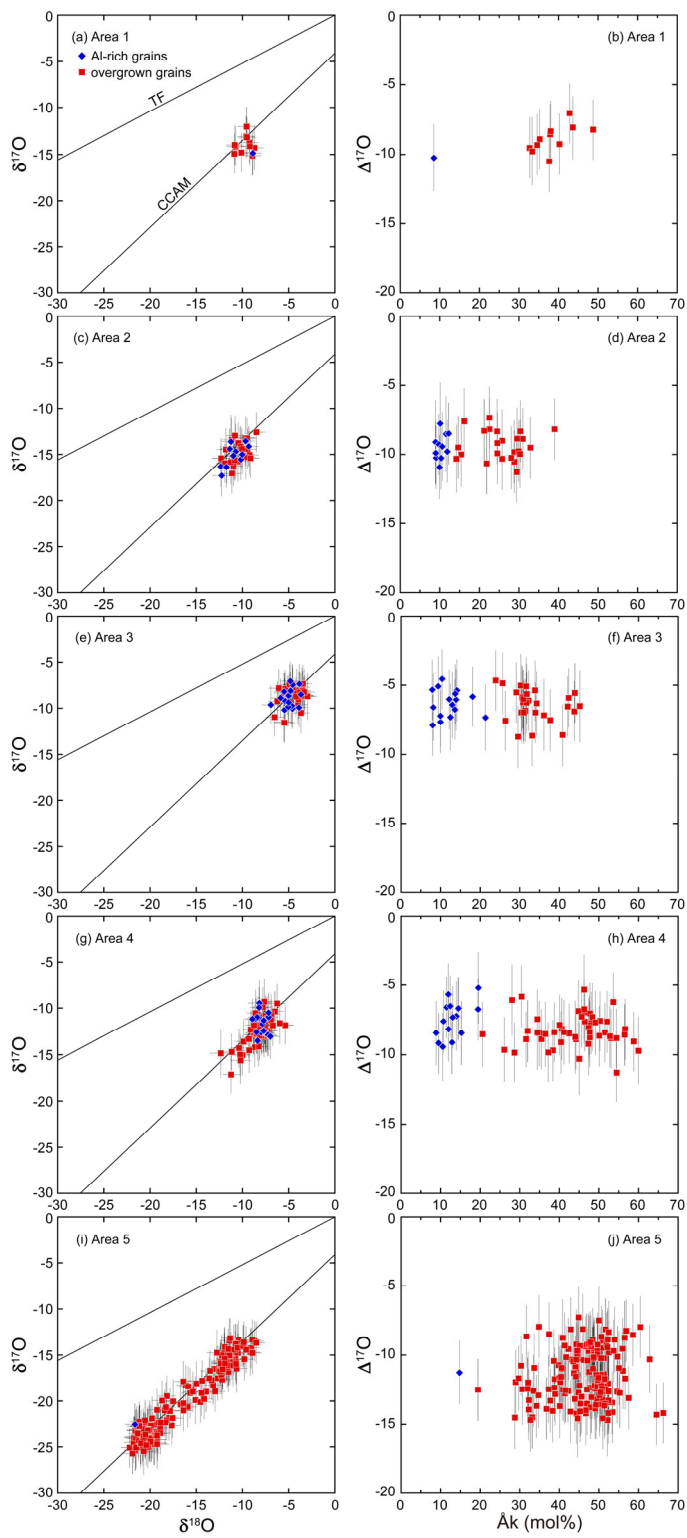
719 masked in gray. (c,d) Zoning of åkermanite content in melilite along the line A–B in (a).
720 (e) MgO⁻ isotope image and (f) $\delta^{18}\text{O}$ quantitative isotope ratio image of the same melilite
721 crystal examined in (c,d). An, anorthite; Fas, fassaite; Mel, melilite; Sp, spinel.
722



723

724 Figure 5. O-isotopic compositions of blocky melilite and spinel in Golfball. Plots of
 725 “overgrown grains” (red squares) include melilite data across boundaries between Al-rich
 726 and overgrown grains (Table S2). Typical error (2σ) is shown. TF, terrestrial fractionation
 727 line; CCAM, carbonaceous chondrite anhydrous mineral line; Mel, melilite; Sp, spinel.

728

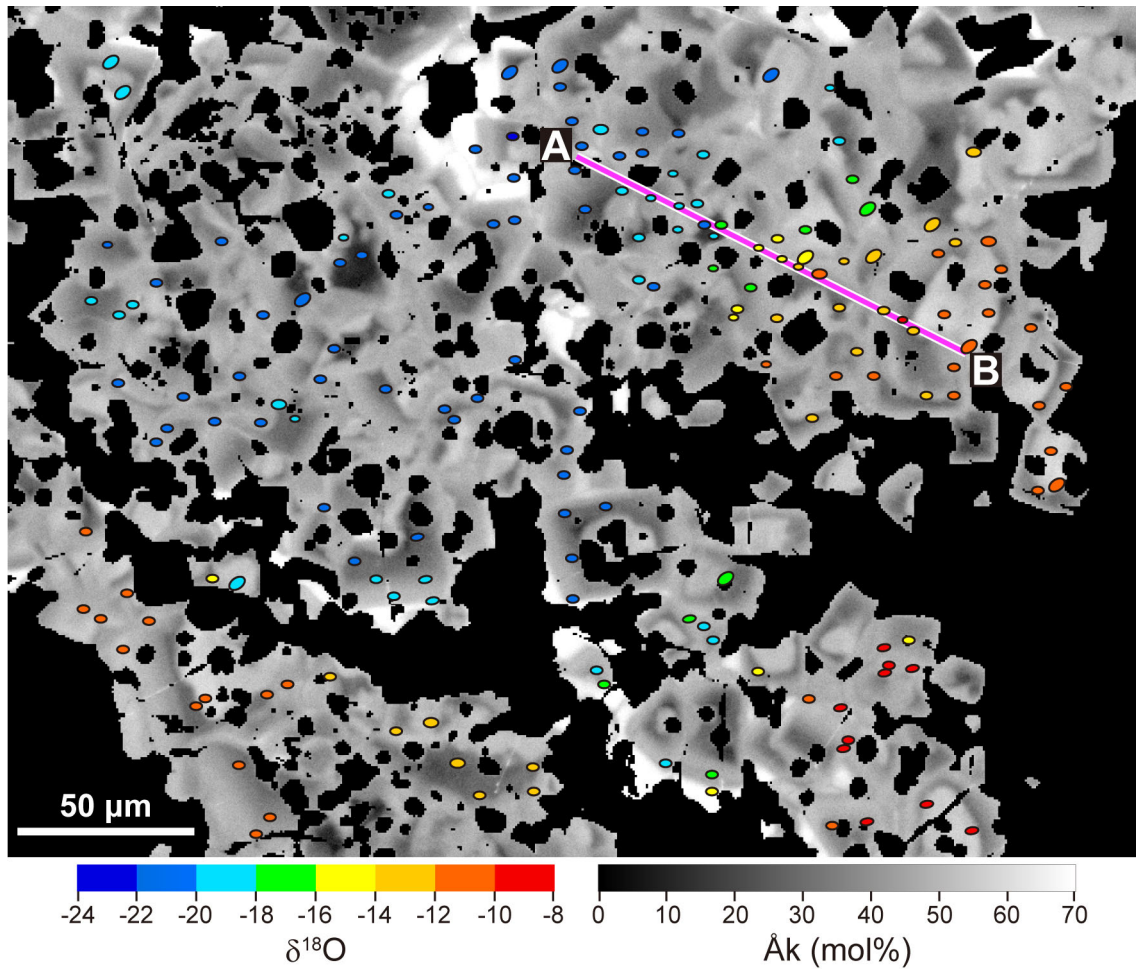


729

730 Figure 6. O-isotopic compositions and their relationships with åkermanite content (\AA k)

731 of Al-rich and overgrown melilite grains in each area of the core. Errors correspond to 2σ .

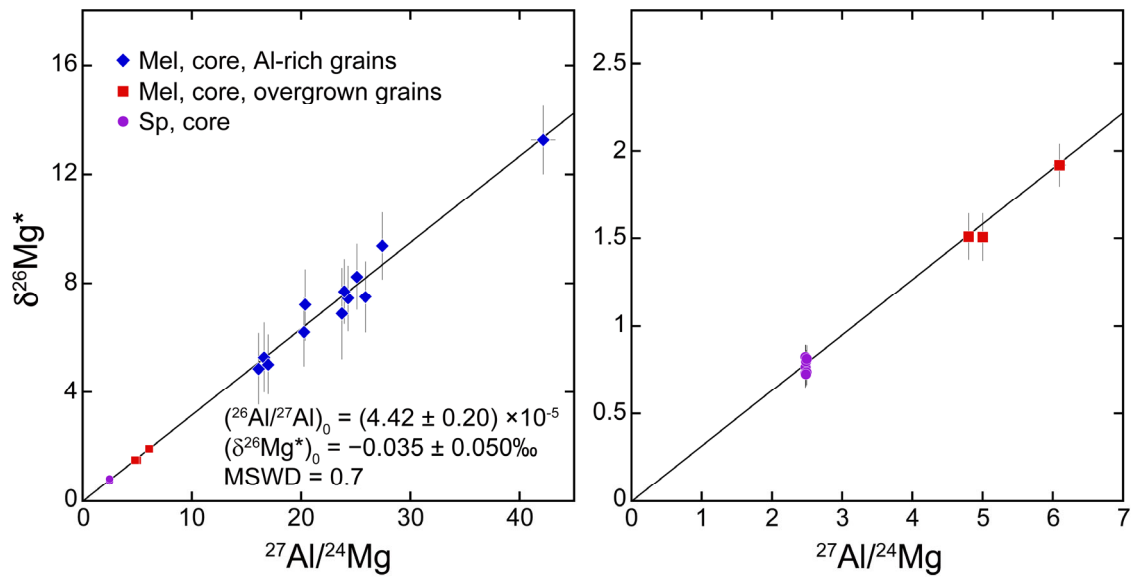
732 TF, terrestrial fractionation line; CCAM, carbonaceous chondrite anhydrous mineral line.



733

734 Figure 7. $\delta^{18}\text{O}$ variations of melilite crystals in area 5 overlaid on quantitative map of
 735 åkermanite content (Åk). Mineral phases except melilite and cracks are masked in black.
 736 Each circle corresponds to spot sizes of *in situ* O-isotope measurements. Data collected
 737 along the A-B traverse are shown in Fig. 9.

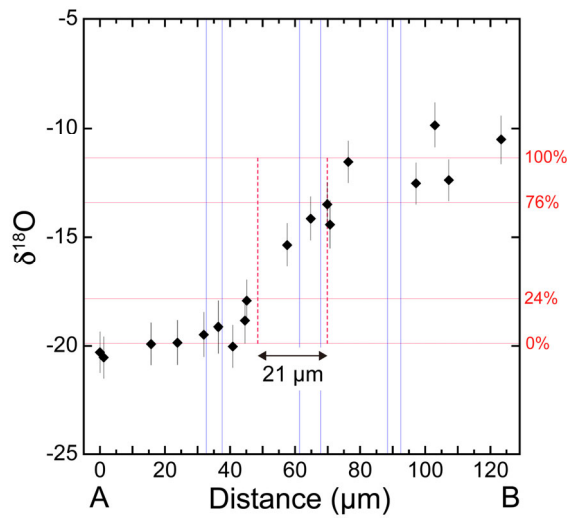
738



739

740 Figure 8. ^{26}Al – ^{26}Mg evolution diagrams for minerals in the core of Golfball, each of
 741 which shows different ranges of $^{27}\text{Al}/^{24}\text{Mg}$ ratio. Isoplot Model 1 (Ludwig, 2003) is used
 742 to fit isochrons. Errors correspond to 2σ . Symbols without error bars exhibit errors smaller
 743 than their symbol sizes. Mel, melilite; Sp, spinel.

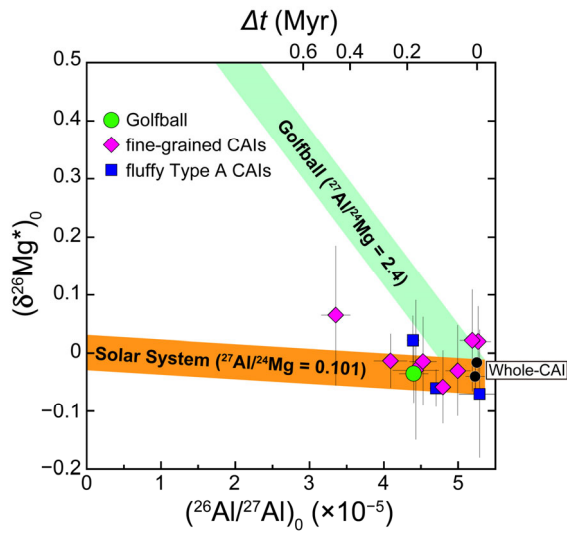
744



745

746 Figure 9. Variations of O-isotopic compositions ($\delta^{18}\text{O}$) along the line A–B in Fig. 7. Spot
 747 data within 4 μm distances from the line are used. Blue vertical lines correspond to
 748 positions of grain boundaries of melilite crystals. A diffusion distance, $2(Dt)^{1/2}$, under the
 749 initial condition of two semi-infinite sources is defined by the width between the 24%
 750 and 76% level (Shewmon, 1963). Errors correspond to 2σ . The spatial resolution of each
 751 point is 2–3 μm , determined by the probe size.

752



753

754 Figure 10. Mg-isotope evolution of Golfball. A calculated Mg-isotope evolution curve for
 755 Golfball from whole-rock CAI $^{26}\text{Al}/^{27}\text{Al}$ and $\delta^{26}\text{Mg}^*$ values (black circles, Jacobsen et
 756 al., 2008; Larsen et al., 2011) is shown as a green-colored area and that for a solar-
 757 composition gas ($^{27}\text{Al}/^{24}\text{Mg} = 0.101$) is shown as an orange-colored area. Colored
 758 diamonds indicate initial $^{26}\text{Al}/^{27}\text{Al}$ and $\delta^{26}\text{Mg}^*$ values for fine-grained CAIs in CV
 759 chondrites (MacPherson et al., 2010, 2012; Kawasaki et al., 2020; Wada et al., 2020) and
 760 colored squares indicate those for fluffy Type A CAIs (MacPherson et al., 2012; Kawasaki
 761 et al., 2019). The $^{27}\text{Al}/^{24}\text{Mg}$ ratio of the Solar System is obtained from Lodders (2003).
 762 Errors correspond to 2σ .